



# Tribocorrosion behaviors of superhard yet tough Ti-C-N ceramic coatings

Y.X. Ou<sup>a,b,1,\*</sup>, H.Q. Wang<sup>b,1</sup>, Q.S. Hua<sup>b,\*</sup>, B. Liao<sup>b</sup>, X.P. Ouyang<sup>b</sup>

<sup>a</sup> Radiation Technology Institute, Beijing Academy of Science and Technology, Beijing 100875, China

<sup>b</sup> Key Laboratory of Beam Technology of Ministry of Education, College of Nuclear Science and Technology, Beijing Normal University, Beijing 100875, China

## ARTICLE INFO

### Keywords:

Ti-C-N coatings  
Superhard and tough  
High power impulse magnetron sputtering  
Tribocorrosion  
Seawater lubrication

## ABSTRACT

Ceramic materials are widely used as protective coatings for marine engineering components in seawater environments due to their high wear and corrosion resistance. However, the applications and lifetimes of these materials have been always limited by the high brittleness of ceramic coatings. Hence, in this work, we report superhard yet tough Ti-C-N coatings with mixed TiC and TiN phases deposited by reactive high power impulse magnetron sputtering. Ti-C-N coatings exhibit a simultaneous superhardness of 40.2 GPa and favorable toughness due to fully dense microstructure and smooth surface morphology. These superhard yet tough Ti-C-N coatings show excellent seawater-lubricating behaviors with an extremely low friction coefficient of 0.03 and mild wear track in 3.5 wt% NaCl aqueous solution. The enhanced tribocorrosion performance is attributed to the increased resistance to crack initiation and propagation, restraining the synergistic actions of wear and pitting corrosion.

## 1. Introduction

With the rapid development of marine industries in recent decades, severe wear and corrosion failures of marine engineering components have caused great economic loss and energy consumption. Anti-wear and anti-corrosion materials and their preparation techniques are highly valued for their environmentally friendly and energy-saving roles. Stainless steel is widely used as a structural component and has good corrosion resistance, but its friction and wear properties are poor [1]. Moreover, tribocorrosion in seawater environments coupled with the negative interactions of wear and corrosion would result in substantial degradation and failure [2,3]. Surface modification and advanced coatings are expected to improve seawater lubrication and the durability of components to ultimately obtain high working performance and long service lifetimes [4,5]. One of the achievable strategies for the enhancement of tribocorrosion performance is the deposition of nanostructured coatings on surface components for combined improvements in seawater lubrication and corrosion resistance [6–11]. In addition, synergistic effects of the hardness and toughness of surface coatings on crack initiation and propagation would make a positive contribution to the enhancement of seawater lubrication and corrosion resistance [12–14].

Lubrication behaviors are closely correlated with the surface

integrity and interface structure of the coated components, in which contact mechanisms are often varied [15]. Many studies have shown how tribo-films formed on contact surfaces act to reduce friction and wear as lubrication layers caused by tribochemical reactions [16,17]. In a seawater environment, however, lubrication behaviors mainly depend on the combined effects of self-lubricating phases on the contact surface, surface integrity, and interface structure due to the formation of only a few tribochemical phases [8,18]. In addition, continuous passive films and surface wettability act on lubrication of the contact surface [19,20]. Moreover, it has been reported that hard yet tough coatings make a key contribution to cooperative deformation for the suppression of crack initiation and propagation [4,12,14].

Cubic transition-metal nitride coatings have the potential to obtain unique properties in terms of hardness, toughness, thermal stability, chemical inertness, and wear and corrosion resistance [2,4]. Nevertheless, the tribocorrosion resistance of coatings is highly desired for seawater lubrication and durability by controlling the surface integrity and interface structure. Cubic CrN coatings deposited on stainless steels using plasma immersion ion implantation showed enhanced resistance to wear and corrosion [5]. However, microcracks induced by friction resulted in multidegradation of the coatings with a typical columnar growth structure, such as intersecting cracks and layer delamination. This is due to microcracks acting as diffusion channels for Cl<sup>-</sup> ions.

\* Corresponding authors.

E-mail addresses: [ouyx16@tsinghua.org.cn](mailto:ouyx16@tsinghua.org.cn) (Y.X. Ou), [q.hua@bnu.edu.cn](mailto:q.hua@bnu.edu.cn) (Q.S. Hua).

<sup>1</sup> The authors contributed equally in this work.

Hence, the refinement or elimination of columnar structures is expected to enhance resistance to corrosion and tribocorrosion by the formation of nanocomposites or multilayer structures [10,11]. Much work has been done on refined CrSiN [21] or TiSiN [9,22]-based nanocomposites and multilayer structures (CrN/TiN [23], CrN/NbN [24], etc.) by the addition of Si and the formation of coherent interfaces. Although tribocorrosion resistance is significantly improved in 3.5 wt% NaCl aqueous solution in terms of a low friction coefficient of 0.1–0.2 and smooth wear tracks [4,6], it is still far from the requirements of seawater lubrication with a friction coefficient below 0.1 [25]. Thus, seawater lubrication would be the only way to achieve durable performance in harsh environments.

Another strategy for enhanced tribocorrosion resistance and seawater lubrication is the addition of C into cubic transition-metal nitride coatings, in which self-lubricating phases and superhard yet tough properties are strongly expected [8–10]. The challenge is how to balance phase control and surface/interface structures with high performance, and then only one or two phases containing C coatings are preferred. (111)-Textured TiCN coatings with a high hardness of approximately 31.6 GPa and Young's modulus of 409.7 GPa synthesized by arc ion plating exhibit limited improvement in tribocorrosion resistance in artificial seawater due to their rough columnar structure and many small microparticles on the surface [26]. Moreover, TiN- and TiCN-based coatings are a remarkable class of cermets in terms of their significant combination of hardness, toughness, strength at elevated temperature, and surface stability in tribology, corrosive or oxidative environments [27]. Hence, superhard yet tough coatings with C content are expected to reduce the concern about solute-ion diffusion channels produced by complete crack penetration of the coating thickness. Moreover, high surface integrity and dense interface structures free of voids, pores, microcracks, etc., greatly benefit tribocorrosion resistance and seawater lubrication [4,9,13]. In addition, the surface wettability of the coatings has a close correlation with the formation of passive films and tribolayers. It has been reported that favorable wettability of the surface would result in a water-lubricated sliding contact surface that would reduce friction and wear due to hydrodynamic films [2]. Meanwhile, sharp decreases in the friction coefficient and wear rate are obtained when CrN/TiN superlattice coatings against Si<sub>3</sub>N<sub>4</sub> counterpart balls and TiCN coatings against SUS440C steel counterpart balls sustain tribocorrosion in artificial seawater due to promising water lubrication on the sliding contact surface [6,14]. Complex interactions between the contact slider and coating surface in the tribocorrosion process lead to a complex tribocorrosion mechanism due to the transient evolution of passive films, tribolayers, and hydrodynamic films [28,29]. Therefore, it is necessary to investigate the tribocorrosion behaviors of superhard yet tough coatings to explore the related mechanisms.

The bulk of the research shows that high power impulse magnetron sputtering (HiPIMS) offers a promising strategy for the preparation of high-performance coatings by high ionization of target species and high plasma density by a series of pulse waveforms in very short time [4,9,14,24]. Hence, in this work, Ti-C-N coatings were deposited using high power impulse magnetron sputtering by reactive sputtering pure Ti targets at various average target powers and substrate biases in mixture gases of acetylene, argon, and nitrogen. Tribocorrosion behaviors of the coatings were investigated in detail to explore the related mechanisms of seawater lubrication of superhard yet tough Ti-C-N coatings.

## 2. Experimental details

### 2.1. Depositions of Ti-C-N coatings

Ti-C-N coatings were deposited using high power impulse magnetron sputtering (HiPIMS) by reactive sputtering a pure Ti target with a purity of 99.95% at various average target powers from 4 to 8 kW and negative substrate bias from –60 to –200 V in a mixture of acetylene, argon and

nitrogen. A rectangular Ti target (449 mm × 75 mm × 6 mm) was installed in the cylindrical chamber (Φ760 mm × 700 mm) structured with a closed field unbalanced magnetron sputtering system. A schematic diagram of the deposition system can be found elsewhere [9]. HiPIMS pulse shapes of target current and voltage for the coatings are shown in Fig. 1. Bright-finished AISI 316L stainless steel and Si(100) coupons (20 mm × 20 mm × 3 mm) were used as substrates for coating deposition. All the substrates were ultrasonically cleaned in acetone and anhydrous alcohol solutions in turn to carefully remove dirt on their surface, and then they were dried with a flow of nitrogen gas. Finally, they were fixed on the substrate holder, maintaining the distance of 120 mm from the target surface. Base pressure in the chamber was pumped to a pressure below  $1 \times 10^{-3}$  Pa. First, the substrates were pre-cleaned for 20 min using an Ar gas ion source at 2 kW, 150 kHz, and a pulse-on time of 26 μs (Pinnacle Plus, Advance Energy). The gas flow rate and negative substrate bias were set at 120 sccm and –200 V, respectively. The deposition time is ranged from 45 to 100 min with the decrease of target power from 8 to 4 kW. Detailed process parameters are shown in Table 1. Approximately 8 μm thick Ti-C-N coatings with a 200 nm TiN adhesion layer were deposited by HiPIMS (Huettinger, Highpulse 4001 G2) at various powers from 4 to 8 kW and various negative substrate biases (Huettinger, Truplasma bias DC 4020 G2) from –60 to –200 V.

### 2.2. Structure and residual stress

The phase composition and crystal structure of Ti-C-N coatings deposited by HiPIMS at the various target powers and negative substrate biases were detected using X-ray diffraction (XRD, X'Pert PRO MPD, PANalytical). The microstructure of the coatings was investigated using field emission scanning electron microscopy (FESEM, S-4800, HITACHI) and transmission electron microscopy (TEM, Philips/FEI CM200). The surface morphology and features of the coatings were studied using atomic force microscopy (AFM, Tosca 400, Anton Paar). The residual stress in Ti-C-N coatings on Si substrates was measured by the Stoney equation as follows [30,31]:

$$\sigma = \frac{1}{6} \frac{E_s t_s}{(1 - \nu_s) t} \left( \frac{1}{R_n} - \frac{2}{R_0} \right) \quad (1)$$

where  $E_s$ ,  $\nu_s$ ,  $t_s$ ,  $t$ ,  $R_0$  and  $R_n$  are Young's modulus, the Poisson ratio, Si substrate thickness, coating thickness, and curvature radii of the Si substrate and coatings, respectively. The results of residual stress are presented in Table 1.

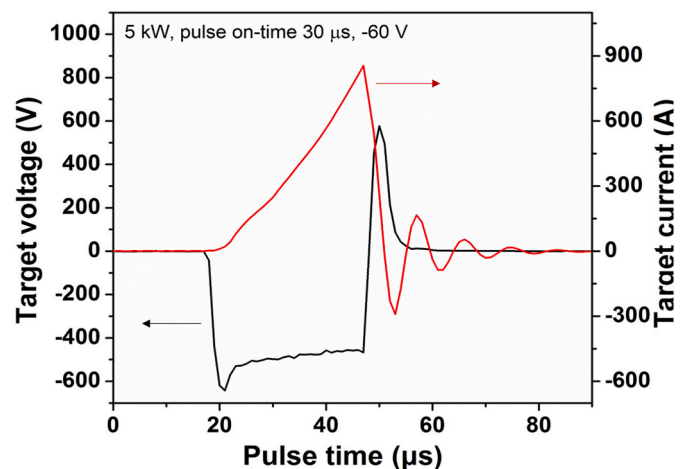


Fig. 1. HiPIMS pulse shapes of the target current and voltage during coating depositions.

**Table 1**

Typical deposition parameters and properties of Ti-C-N coatings deposited by high power impulse magnetron sputtering.

Bias [V]	P <sub>mean</sub> [kW]	V <sub>peak</sub> [V]	I <sub>peak</sub> [A]	f [Hz]	L [μm]	G <sub>(111)</sub> [nm]	σ [GPa]	W <sub>r</sub> [ $\times 10^{-6}$ mm <sup>-3</sup> N <sup>-1</sup> m <sup>-1</sup> ]
-60	4	786	128	855	7.8	16.8	-1.3	3.52
-60	5	498	287	1328	8.1	16.6	-1.5	0.13
-60	8	320	326	1543	8.3	15.1	-4.1	3.34
-100	5	501	289	1334	8.2	15.8	-2.4	0.29
-150	5	499	288	1332	8.1	14.9	-3.1	1.22
-200	5	502	292	1327	7.9	14.2	-3.8	6.87

Note: P<sub>mean</sub> – Average target power; V<sub>peak</sub> – Peak target voltage; I<sub>peak</sub> – Peak target current; f – Frequency; L – Coating thickness; G – Grain size based on Ti-C-N (111) peak; σ – Residual stress; W<sub>e</sub> – Elastic recovery; W<sub>r</sub> – Specific wear rate.

### 2.3. Mechanical properties, adhesion and wettability

The hardness (H) and effective Young's modulus (E\*) of Ti-C-N coatings deposited by HiPIMS at various target powers and negative substrate biases were determined using a nanoindenter (Nanotest system, NanoTest, Micro Materials) equipped with a Berkovich diamond indenter. An indentation depth of less than 10% of the coating thickness was set to reduce the substrate effect. In addition, in our case, 16 points were detected to calculate the mean hardness and effective Young's modulus. Young's modulus was calculated using the formula  $E^* = E / (1 - \nu^2)$ . The H/E\* and H<sup>3</sup>/E\*<sup>2</sup> ratios were calculated. The adhesion of the Ti-C-N coating between substrates was studied by a Rockwell C indentation test (HRC) equipped with a 200 μm radius HRC indenter under a standard load of 150 kg. The HRC adhesion level of coatings/substrates was determined according to FESEM images of Rockwell C indentations according to VDI guidelines 3198, (1991) [4,32].

The fracture toughness K<sub>IC</sub> of Ti-C-N coatings was determined using the length of the radial cracks of the Vickers indentations made by a microhardness tester (MMT-X, Matsuzawa) under an applied load of 0.1 N [33]. In our case, there are no radial cracks along Vickers indentations (inserted in Fig. 6a and b), indicating favorable toughness. Gas-liquid-solid interfaces will form when droplets of distilled water are deposited on the coating surface. The wettability of the coating surface was detected by measuring contact angles using static drop micro-observation on a contact angle analyzer (Data Physics OCA20) with a water droplet volume of 4 mL at ambient temperature. The mean value of the contact angle was calculated for at least three different positions on the coating surface. The schematic diagram of the calculated contact angles based on the classical Young's equation as follows [34]:

$$\cos\theta = \frac{\gamma_{sv} - \gamma_{sl}}{\gamma_{lv}} \quad (2)$$

where solid-gas, solid-liquid and liquid-gas interfacial tensions are represented by  $\gamma_{sv}$ ,  $\gamma_{sl}$  and  $\gamma_{lv}$ , respectively. Liquid-gas interfacial tension is always considered surface tension.

### 2.4. Tribocorrosion performance

The tribocorrosion performance of Ti-C-N coatings deposited using HiPIMS at various target powers and negative substrate biases in 3.5 wt % NaCl aqueous solution was evaluated by a linear reciprocating tribometer integrated with a three-electrode cell configuration (MFT-EC4000, HUAHUI) against Si<sub>3</sub>N<sub>4</sub> counterpart balls (Φ 6 mm) at a sliding time of 60 min. More detailed information about the tribocorrosion equipment and schematic diagram can be found in Rf. [4]. The reciprocating length, frequency, and normal load were 5 mm, 1 Hz, and 5 N, respectively. In the process of tribocorrosion tests, the in situ electrochemical response was investigated in terms of the change in open circuit potential (OCP) and coefficient of friction as a function of sliding time to explore the evolution of passive films. The surface morphology of wear tracks was observed by optical microscopy to study tribocorrosion mechanisms. Then, a Taylor Hobson surface profilometer was used to measure the wear track profile to calculate the specific tribocorrosion

rate of the worn samples, shown in Table 1.

## 3. Results and discussion

### 3.1. Depositions, chemical composition and structure

Ti-C-N coatings with a thickness of approximately 8 μm were deposited by HiPIMS at various target powers from 4 to 8 kW and negative substrate biases from -60 to -200 V in a closed field unbalanced magnetron sputtering system in a mixture gas of acetylene, argon, and nitrogen. The typical HiPIMS pulses are shown in Fig. 1. At a constant width of the micropulse, the increased average HiPIMS power indicates an increased number of micropulses, i.e., the frequency was increased. Thus, the increased average power density produces a much greater amount of ionized target species to form a high density of plasma. With an increase in negative substrate bias, ion bombardment into the substrate surface was enhanced by the increased impact energy of energetic ions in the plasma. In addition, ion bombardment has a sensitive correlation with film growth in terms of the migration of adatoms and growth of metastable phases in a nonequilibrium condition. A strong impact on the surface always results in a rough surface morphology along with an increased sputtering yield and residual stress [35–37]. Hence, optimized reactive HiPIMS depositions with the appropriate target sputtering power and negative substrate bias benefit high-performance coatings.

Fig. 2 shows XRD patterns of Ti-C-N coatings deposited by HiPIMS at various powers and substrate biases. As shown in Fig. 2, (111) and (222) peaks with broadening widths overlapping between the TiN and Ti-C-N phases are detected in the XRD patterns of Ti-C-N coatings, except for the diffraction peaks labeled "SS" from 316L stainless steel substrates and Ti adhesion layers. The diffraction peaks from TiN and Ti-C-N are

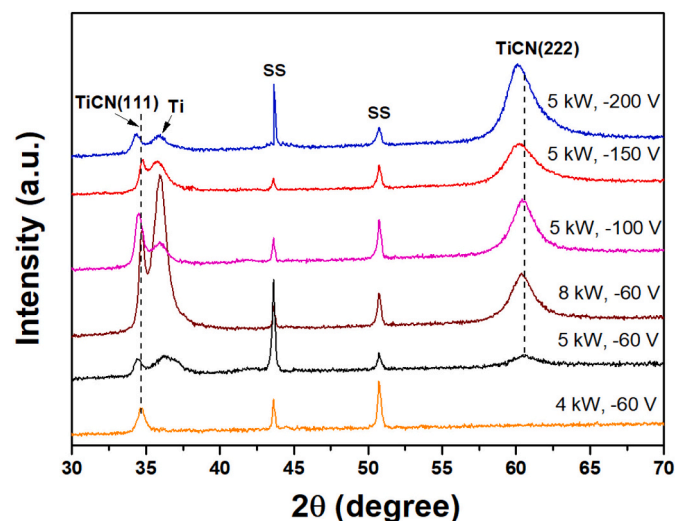


Fig. 2. XRD patterns of Ti-C-N coatings deposited by HiPIMS at various powers and substrate biases.

difficult to completely distinguish due to their same face-centered structure and similar atomic radii. In addition, the broadening width and shifting toward the low angle of the (111) and (222) peaks indicate significant refinement of grains. At 4 kW and  $-60$  V, the coatings are dominated by a cubic Ti-C-N phase even at a lower density of Ti plasma due to a wide range of chemical compositions of the  $\text{TiC}_x\text{N}_{1-x}$  ( $0 < x < 1$ ) phase [38,39]. When the negative substrate bias is fixed at  $-60$  V, the (111)-textured coatings are gradually obtained with increasing target power from 4 to 8 kW. It is noted that the coatings deposited at 4 kW and  $-60$  V show random orientations of (111) and (220). According to our previous studies, the disappearance of the preferred orientation is attributed to the formation of ultrafine grains [40,41].

Fig. 3a presents TEM images of the cross-sectional morphologies of Ti-C-N coatings deposited by HiPIMS at 5 kW and  $-60$  V. As shown in Fig. 3a, Ti-C-N coatings are composed of a Ti adhesion layer, TiN transition layer, and Ti-C-N coatings. No holes and gaps have been detected. Both Ti and TiN layers possess dense columnar structures, but Ti-C-N coatings have highly dense and discontinuous nanocolumnar structures. Moreover, there are also highly dense interfaces, so no obvious interfaces between layers are observed. Hence, according to the structure zone diagram (SZD) modified by Anders [42], the fine nanograins with a preferred orientation of coatings belong to Zone T. The inserted selected area electron diffraction (SAED) patterns reveal distinct diffraction rings assigned to (111), (200) and (220) reflections from the fcc crystal structure of Ti-C-N coatings, including Ti(C,N) and TiN, due to the small difference in their lattice constants. These agree well with the XRD results of Fig. 2.

As shown in Fig. 3b, the high-resolution TEM image of the selected red frame in Fig. 3a presents a dense microstructure without distinct grain boundaries. The (111) and (220) reflections for TiN and Ti(C,N) are detected in the selected area electron diffraction (SAED) patterns inserted in Fig. 3a. Fig. 3c shows uniform elemental distributions of Ti, C, and N in the selected red frame of Fig. 3a detected by EDS lateral scanning. It is clearly observed that much more elemental Ti is present than N and C, indicating that there is sufficient Ti to react with N and C

to form TiN and Ti(C,N) in TiCN coatings. Based on XRD and XPS results, it is also noted that there are no halos and a lesser content of C than Ti and N, revealing few amorphous  $\text{CN}_x$  phases in the coatings. The increased HiPIMS target sputtering power and appropriate substrate bias are efficient in generating a high ionization rate of target species and increasing metal ion bombardment [40,43]. Thus, a mass of momentum transfer between the growing film and the incoming metal ions results in the refinement of the microstructure with a less coarse columnar structure. Hence, high surface integrity, including high density, freedom from defects, and uniformity is obtained for Ti-C-N coatings deposited by HiPIMS under appropriate conditions (5 kW and  $-60$  V).

XPS core level spectra of Ti 2p, C 1s, and N 1s were determined to analyze the chemical bonding state of the elements in Ti-C-N coatings deposited by HiPIMS at 4–8 kW and  $-60$  V, as shown in Fig. 4. At 4 kW, the asymmetric Ti 2p spectrum is composed of two main peaks originating from Ti 2p<sub>3/2</sub> and Ti 2p<sub>1/2</sub> peaks at binding energies (BEs) of 457.1/463.1 eV, 455.9/461.8 eV and 458.4/464.4 eV (Fig. 4a), indicating 3 possible species for Ti-(C,N), Ti-N and Ti=O bonds, respectively [38,40,44]. No Ti-C bonds are detected in the coatings. Fig. 4b shows a broadened peak overlapped by four peaks in the C 1s spectra at 282.9 eV for C-(Ti,N), 284.5 eV for sp<sup>2</sup>C-C/C-N, 285.4 eV for sp<sup>3</sup>C-C/C-N and C-O bonds at 286.7 eV. For the N 1s spectra (Fig. 4c), a main asymmetric peak with two shoulder peaks is obtained, indicating N-(C, Ti) at 396.5 eV, TiN at 397.3 eV, sp<sup>2</sup>C-N at 398.4 eV and sp<sup>3</sup>C-N at 399.9 eV. From these it is inferred that TiCN and TiN phases form in the coatings, while the TiC phase forms with difficulty at plasma temperature conditions (lower sputtering power) due to its higher formation energy compared with those for Ti(C,N) and TiN [38].

A small C-O signal results from surface contamination. With an increase in the target sputtering power, Ti-C bonds appeared, and their intensity increased, which revealed the formation of the TiC phase (Fig. 4d–i). Thus, Ti-C-N coatings are mainly composed of Ti(C,N) and TiN phases, which agrees with the XRD results in Fig. 2. Based on the XPS results above, Ti ions easily react with N to form TiN, while C atoms

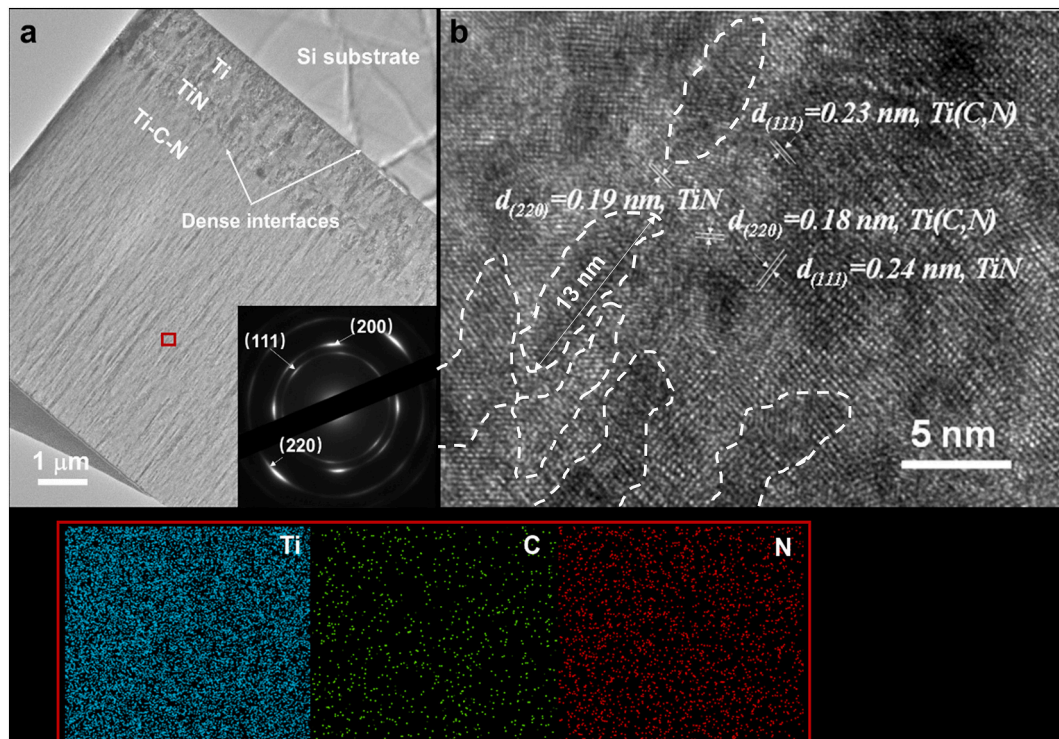


Fig. 3. TEM investigations of cross-sectional morphologies of Ti-C-N coatings deposited by HiPIMS at 5 kW and  $-60$  V: a, bright field image with SAED patterns inserted; b, high-resolution TEM images of the selected red frame in a; c, uniform elemental distributions of Ti, C and N in the selected red frame of a.

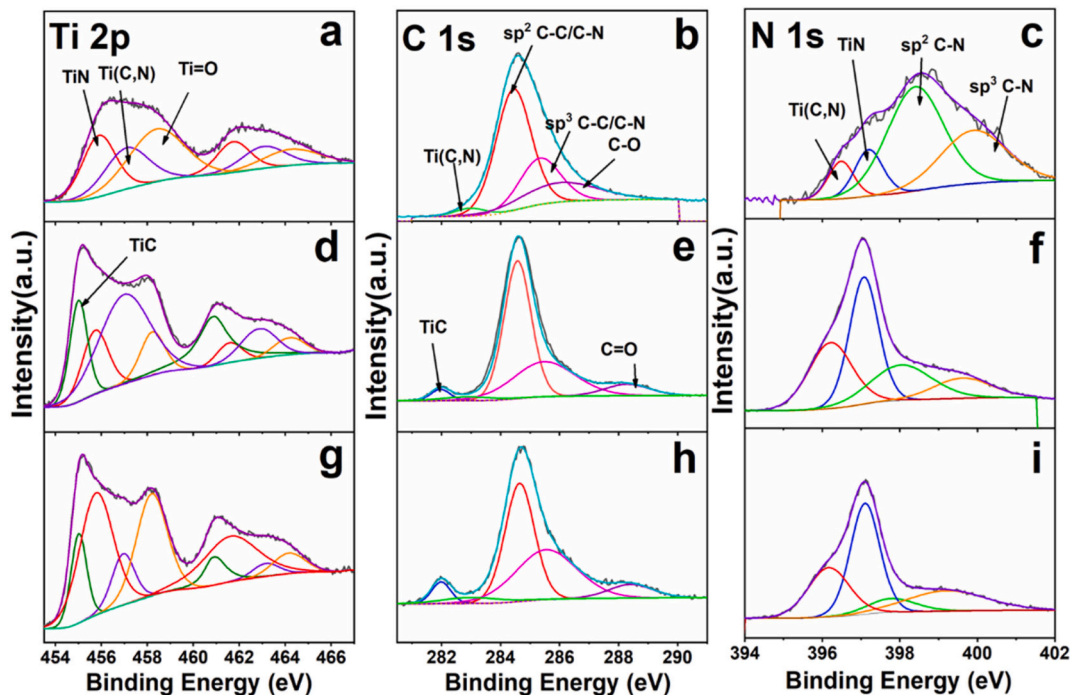


Fig. 4. XPS spectra of Ti-C-N coatings deposited by HiPIMS at 4-8 kW and -60 V.

exit the TiN lattice point as interstitial atoms to form Ti(C,N). A small amount of  $sp^2$  C reacts with N to form a  $CN_x$  phase. The increased sputtering power produces more Ti ions to promote the formation of TiN, which would reduce the amount of amorphous  $sp^2$  C and  $CN_x$  phases in the coatings. Therefore, Ti-C-N coatings mainly contain Ti(C,N) and TiN, as well as a small amount of  $CN_x$  phases. Ti-C-N coatings are easily reactively deposited to form Ti(C,N) and TiN [44], while amorphous  $CN_x$  phases are generated under conditions of higher C content [38].

### 3.2. Surface morphologies and wettability

As reported, surface integrity, including a smooth surface, a highly dense microstructure, the absence of defects, low residual stress, and high uniformity, is vital for high-performance coatings [4,45]. The surface morphologies of Ti-C-N coatings deposited by HiPIMS at various target powers and negative substrate biases were investigated using AFM. As shown in Fig. 5a, rough surface morphologies with a large package of particles and distinct gaps between particles boundaries are observed for the coatings deposited at 4 kW and -60 V. A smooth surface morphology with smaller grains is formed at 5 kW and -60 V due to the increased number of energetic ions and ion bombardment, leading to the migration of adatoms to promote film growth (Fig. 5b). At 8 kW and -60 V, the increased ion bombardment results in a decrease in grain size, but a rough surface with craters is also obtained on the coating surface (Fig. 5c). Meanwhile, the residual stress in the coatings sharply increases from -1.3 to -4.1 GPa. When the HiPIMS sputtering power was fixed at 5 kW, the evolution of the surface morphology changed from a dune shape to foothill features with increasing negative substrate bias from -60 to -200 V, as shown in Fig. 5d-f. Thus, strong ion bombardment results in a rougher surface with craters and foothills. It is inferred that the appropriate energetic ion flux and ion bombardment were closely related to the target power and that substrate bias promoted high surface integrity and low residual stress by controlling the migration of surface adatoms. The combined improvement is attributed to the precise control of the micropulse of HiPIMS and reactive deposition conditions of the coatings [42,46].

Tribological hard coatings have been widely used in the field of

marine engineering as protective coatings [24,47]. Hence, their surface and interface features have a key influence on the performance due to surface hydrophilicity and hydrophobicity [48]. The surface wettability reveals unique properties of the gas-liquid-solid interfaces, which strongly depend on surface nanostructures and roughness attributed to the varied surface free energy [49,50]. Surface wettability is thus of interest in the field of tribocorrosion behaviors working in aqueous solution environments. The wettability can be characterized by surface free energy using the measurement of contact angles. Thus, Fig. 5g-m illustrates the contact angles of droplets of distilled water on the surface of Ti-C-N coatings deposited using HiPIMS at various target powers and negative substrate biases. Fig. 5g presents a schematic diagram of the contact angles. As shown in Fig. 5h-j, an increase in the target power results in a decrease in the contact angle from  $64.6^\circ$  to  $42.4^\circ$ , followed by an increase to  $55.2^\circ$ . The increased negative substrate bias results in an increased contact angle from  $56.7^\circ$  to  $81.5^\circ$  (Fig. 5k-m). The evolution of the surface morphology of Ti-C-N coatings is responsible for changes in the contact angle. It is clearly seen from the surface morphology that the variation in contact angle is induced by the surface roughness. The Ti-C-N coatings deposited at 5 kW and -60 V with smooth surface morphology exhibit good wettability with a low contact angle of  $42.4^\circ$ .

### 3.3. Mechanical properties and adhesion

Fig. 6 exhibits the hardness (H), effective Young's modulus ( $E^*$ ),  $H/E^*$ , and  $H^3/E^{*2}$  ratios of Ti-C-N coatings deposited using HiPIMS at various target powers and negative substrate biases. As shown in Fig. 6a-d, at 4 kW and -60 V, the values of H,  $E^*$ ,  $H/E^*$ , and  $H^3/E^{*2}$  are 30.5 GPa, 332.4 GPa, 0.092, and 0.257, respectively. With target power increasing to 8 kW, H and  $E^*$  gradually increase to 42.8 GPa and 437.4 GPa, respectively. However,  $H/E^*$  and  $H^3/E^{*2}$  reach their highest values of 0.104 and 0.433 at 5 kW, respectively. Hence, when the target power was fixed at 5 kW, the substrate bias was increased from -60 to -200 V, and H and  $E^*$  gradually increased to 44.2 GPa and 476.3 GPa, respectively. However, under these same conditions,  $H/E^*$  and  $H^3/E^{*2}$  show decreases to 0.093 and 0.381, respectively. In addition, the micro-indentation images inserted in Fig. 6a, b under a load of 0.1 N show that

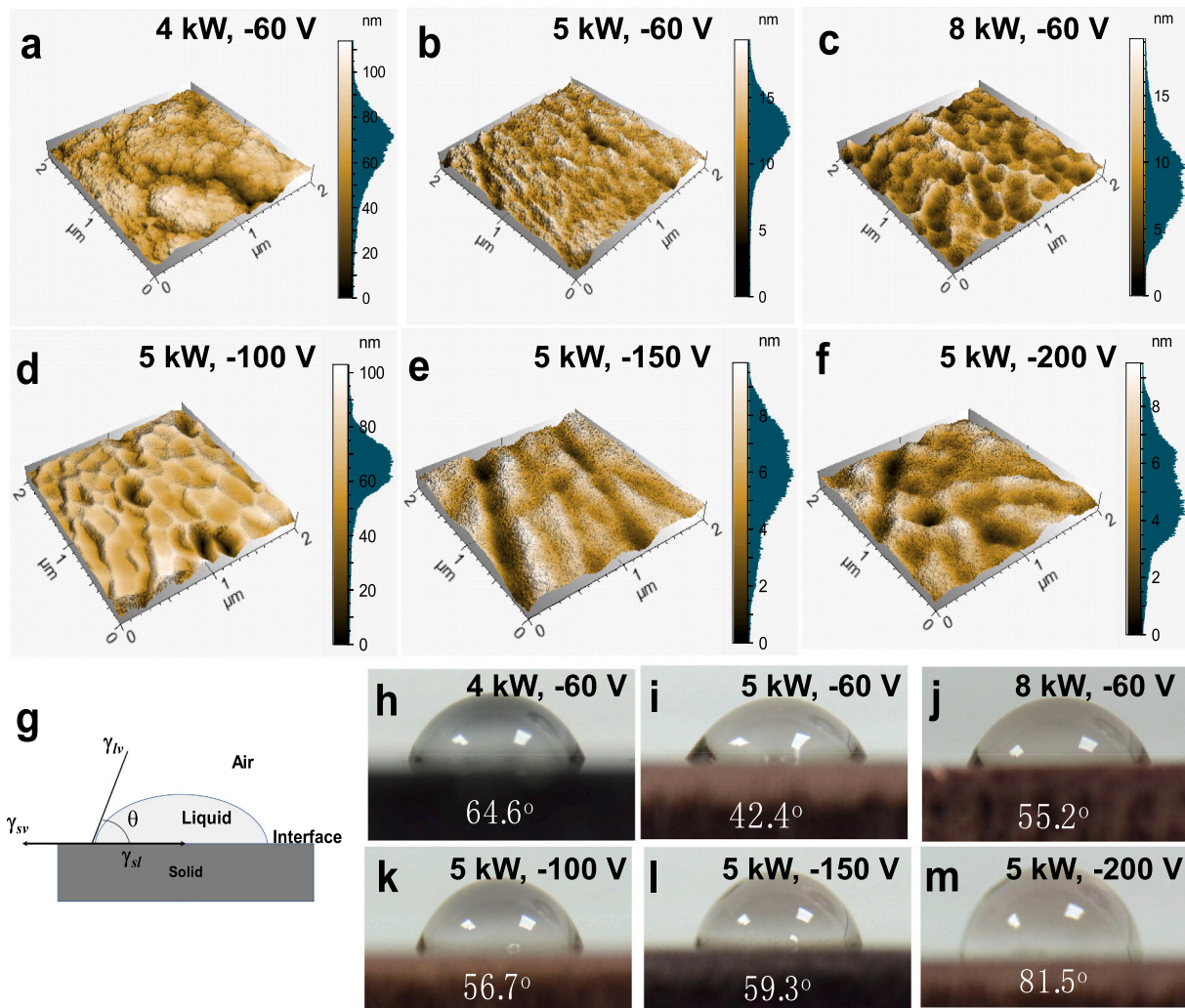


Fig. 5. Surface morphologies and contact angles of Ti-C-N coatings deposited by HiPIMS at various target powers and negative substrate biases: a-f, surface morphologies; g, contact angle formulas in air-liquid-solid interface; h-m, contact angle of droplets of distilled water.

the coatings possess excellent fracture toughness. It is clearly seen that no radial cracks of Vickers indentations were observed with increasing HiPIMS power and negative substrate bias. At 5 kW and  $-60$  V, the coatings have smooth and smaller indentations, indicating a higher fracture toughness [12–14].

In general, hardness and toughness are difficult to simultaneously achieve, but heterogeneous interfaces are gradually introduced into nanomaterials to enhance them as interfacial engineering rapidly develops. Hence, hard yet tough and flexible hard multilayer or nanocomposite coatings formed by nanocrystalline and amorphous materials, and their interfaces exhibit excellent friction and wear properties [5,13,40]. Moreover, superhard yet tough coatings are always expected by precise control of the chemical composition and microstructure to achieve the combined improvement of hardness and toughness [12]. Thus, it is demonstrated that Ti-C-N coatings deposited at 5 kW and  $-60$  V exhibit superhard yet tough features. Moreover, the relationship between the mechanisms of producing these superhard yet tough features is attributed to the blocking of dislocation motion across interfaces at boundaries between dense and refined grains, as well as the contribution of the solution strengthening of Ti(C,N) with C interstitial atoms in TiN. In addition, the fully dense composite structure with refined Ti(C,N) and TiN grains promotes enhanced cohesion strength.

The combined improvements in hardness, toughness, and cohesion/adhesion are essential for hard coatings used in wear and corrosion applications. Thus, Rockwell C indentations under a standard load of

150 kg were used to determine the cohesion/adhesion between the coatings and substrates by the large deformation of the coatings along with substrates. In addition, the enhanced hardness and toughness also account for the improved adhesion between superhard yet tough coatings and 316L stainless steel substrates due to their close correlations with  $H$ ,  $H/E^*$  and  $H^3/E^{*2}$  [4,23,40].

Fig. 7 reveals Rockwell C indentations for the Ti-C-N coatings deposited using HiPIMS at various target powers and negative substrate biases. According to VDI 3198 rule [32], the criteria of each level (HF1–4) is determined by brittle radial cracks and outside edge delamination of hard ceramic coatings. However, in our cases, there are few radial brittle cracks along indentations in Ti-C-N coatings, indicating the increased fracture toughness as discussed in Fig. 6. Hence, according to cracks and delamination along outside edge indentation, HF adhesion level is defined as HF1 (few cracks and delamination), HF2 (Small cracks and delamination), HF3 (Initial cracks and delamination), HF4 (Increased cracks and delamination), HF5 (Large delamination) and HF6 (Total delamination). With an increase in target power from 4 to 8 kW, the adhesion shows an initial increase from HF4 to HF1, followed by a decrease to HF3. The adhesion level presents a gradual decrease from HF1 to HF3 with increasing substrate bias from  $-60$  to  $-200$  V. In addition, the residual compressive stress shows an increase from  $-1.3$  to  $-4.1$  GPa with increasing target power and from  $-2.4$  to  $-3.8$  GPa with increasing substrate bias, respectively (as shown in Table 1). It is noted that the coatings with high  $H$ ,  $H/E^*$ , and  $H^3/E^{*2}$  exhibit a reduction in

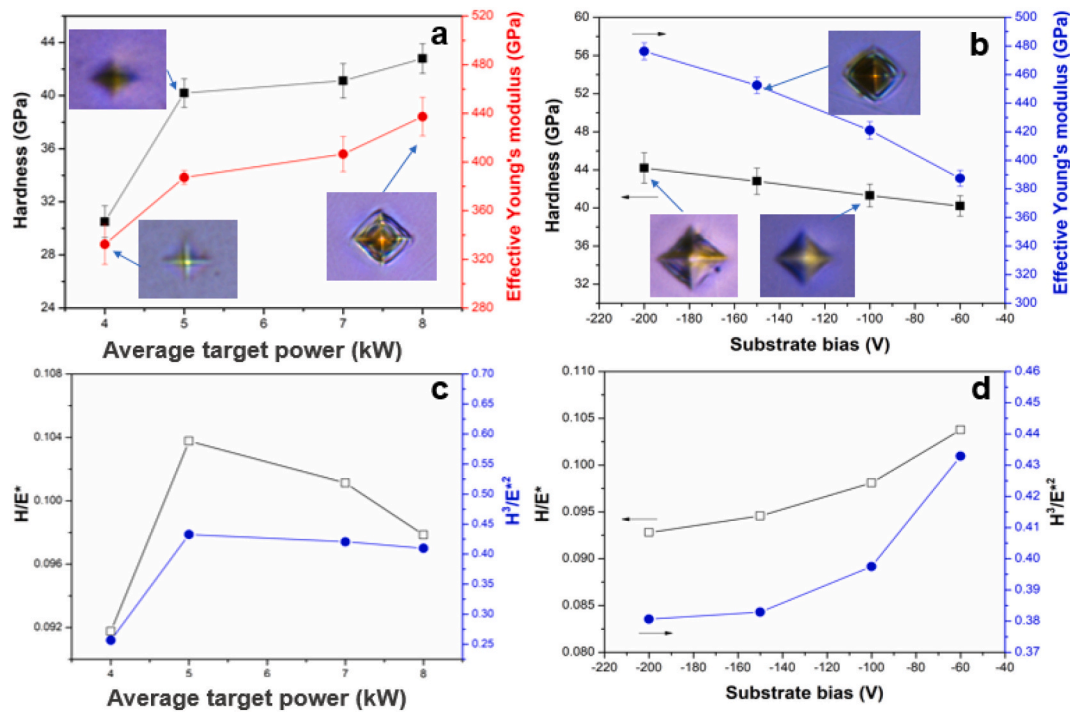


Fig. 6. a, b, Hardness (H), effective Young's modulus ( $E^*$ ); c,d,  $H/E^*$ , and  $H^3/E^{*2}$  ratios of Ti-C-N coatings deposited by HiPIMS at various target powers and negative substrate biases. Micro-Vickers indentations inserted in a and b.

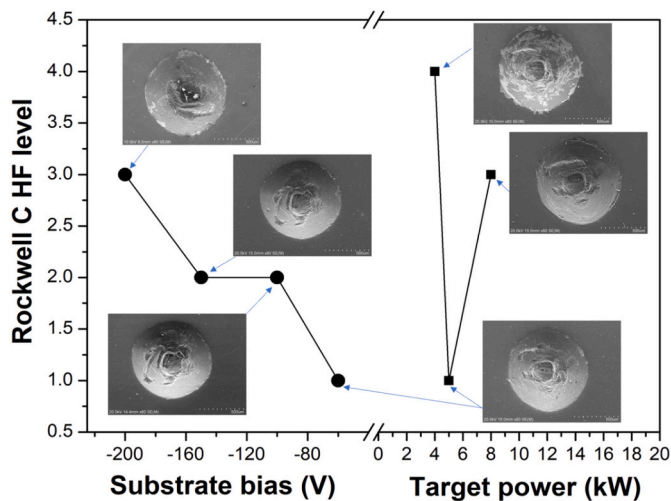


Fig. 7. Rockwell C adhesion level and indentations of Ti-C-N coatings deposited using HiPIMS at various target powers and negative substrate biases.

cracking at the both the edge and the inside of each indentation, corresponding to the HF adhesion level and cohesion, respectively, due to the enhanced cracking resistance. Similar results have also been reported for CrN/TiN superlattice coatings [23] and TiAlSiN nanocomposite coatings [40] deposited by deep oscillation magnetron sputtering, known as an alternative HiPIMS technique. The improvement in cohesion/adhesion of coatings is ascribed to the enhanced H,  $H/E^*$ , and  $H^3/E^{*2}$  due to smooth surface morphology, highly dense microstructure, and low residual stress.

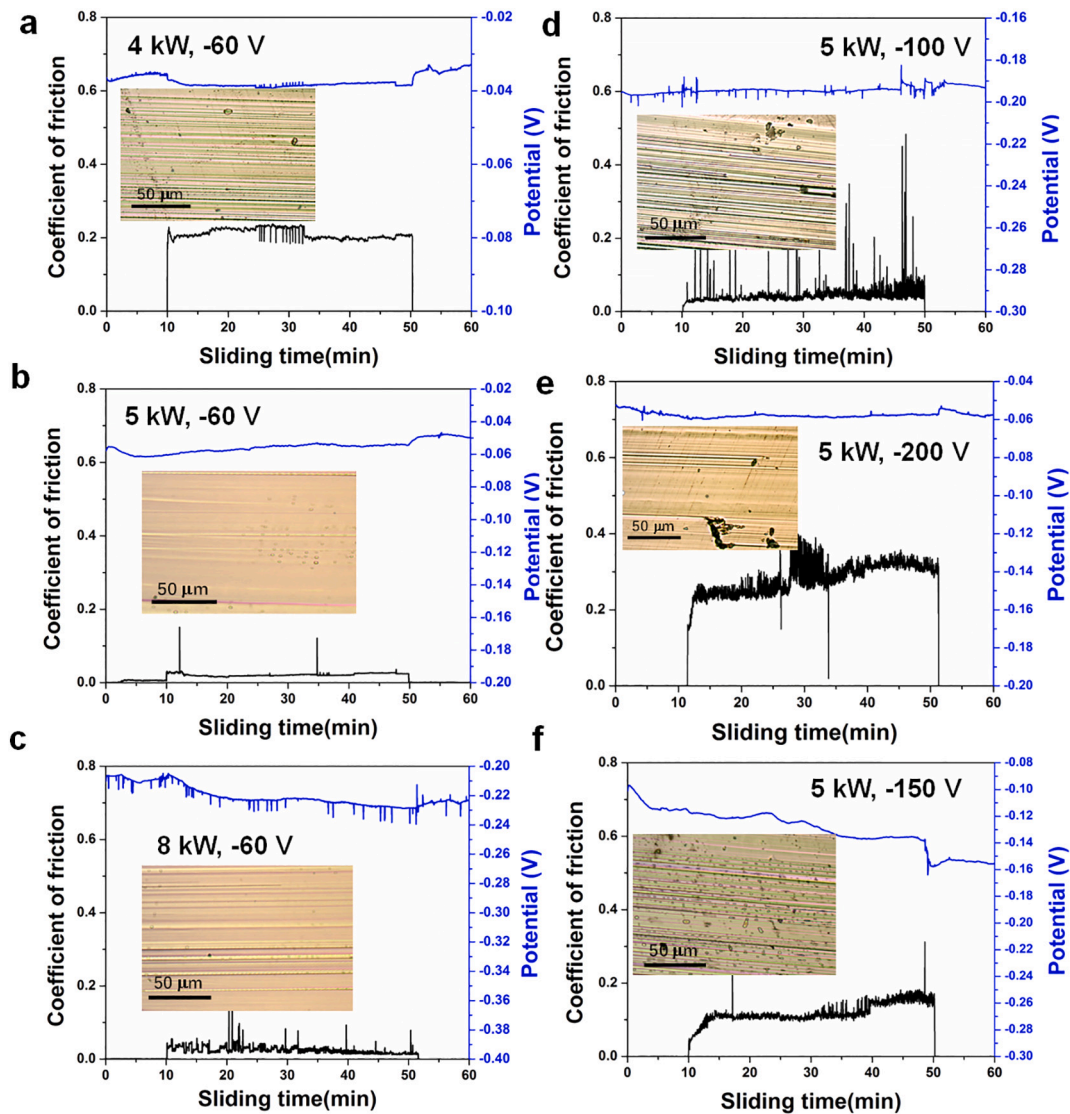
### 3.4. Tribocorrosion resistance

Fig. 8 presents the tribocorrosion behaviors in a 3.5 wt% NaCl aqueous solution of Ti-C-N coatings deposited using HiPIMS at various

target powers and negative substrate biases compared with those for hard coatings. The tribocorrosion resistance of the coatings is evaluated by the instantaneous coefficient of friction (COF), in situ response of open circuit potential (OCP), and worn surface morphologies. As shown in Fig. 8a, fluctuating COFs and OCPs at 4 kW and  $-60$  V are observed during tribocorrosion tests, and the average values are 0.21 and  $-0.036$  V, respectively. This is because the coatings suffer from severe abrasive wear leading to distinct long grooves parallel to the friction direction. These result from hard wear debris polishing the sliding contact surface. In addition, low surface wettability is not useful for decreasing wear and friction. Large furrows on the worn surface is attributed to low abrasive wear resistance due to relatively low  $H/E^*$ , and  $H^3/E^{*2}$ . Note that no macrocracks are observed on the worn surface during sliding wear. Hence, the diffusion distance of  $Cl^-$  in tribocorrosion is limited between the sliding contact surface and sublayer. Thus, severe polishing and deformation result in microcracks in the sublayer of the coatings owing to the dense microstructure and high cohesion/adhesion. The calculated specific wear rate is  $3.52 \times 10^{-6} \text{ mm}^{-3} \text{ N}^{-1} \text{ m}^{-1}$ .

When the average target power is increased to 5 kW, a sharp decrease to 0.04 of the COF and a slight decrease to  $-0.055$  V of OCP are obtained, as shown in Fig. 8b. At the beginning of 10 min, OCP is higher  $-0.05$  V due to the formation of passive films. Then, the OCP gradually decreases and reaches a stable value of approximately  $-0.055$  V during sliding wear, revealing durable passive films formed on the contact surface. The worn surface presents smooth and clean morphologies along with shallow grooves, indicating mild abrasive wear. The calculated specific wear rate is  $1.3 \times 10^{-7} \text{ mm}^{-3} \text{ N}^{-1} \text{ m}^{-1}$ .

Superhard yet tough Ti-C-N coatings exhibit high resistance to elastic and plastic deformation to reduce the formation of microcracks and polishing. In addition, superhard yet tough coatings with high cohesion/adhesion possess high cooperative deformability, which reduces cracking and adhesion failure. This produces high surface integrity, building a strong barrier against the acceleration of tribocorrosion failure due to  $Cl^-$  ion diffusion. Moreover, the high surface wettability promotes uniform water films and passive films formed at the sliding contact surfaces, reducing friction and wear. As we reported in our



**Fig. 8.** Tribocorrosion behaviors of Ti-C-N coatings deposited using HiPIMS at various target powers and negative substrate biases in 3.5 wt.% NaCl aqueous solution.

previous works, the enhanced surface integrity and interface structure contribute to the combined improvement of hardness and toughness, leading to high resistance to wear, corrosion, and tribocorrosion [4,14,26]. At 8 kW, although the COF is still approximately 0.05, it exhibits a quite unstable tendency. In addition, oscillating changes in corrosion potential are detected, and the average value is approximately  $-0.23$  V (Fig. 8c). The calculated specific wear rate is  $3.34 \times 10^{-6} \text{ mm}^{-3} \text{ N}^{-1} \text{ m}^{-1}$ . With an increase in substrate bias from  $-60$  to  $-200$  V (Fig. 8d–f), the COF and OCP exhibit a sharp fluctuation and increase to 0.34 and  $-0.05$  V, respectively, due to severe abrasive wear resulting in cracking and adhesive failure during tribocorrosion tests. The calculated specific wear rate increases from  $0.29 \times 10^{-6}$  to  $6.87 \times 10^{-6} \text{ mm}^{-3} \text{ N}^{-1} \text{ m}^{-1}$ . Meanwhile, the deterioration of Ti-C-N coatings would be accelerated owing to high residual stress and surface defects caused by ion bombardment with increasing substrate bias. For traditional lubricating materials, DLC-based coatings exhibit good tribocorrosion resistance with a low coefficient of friction of 0.036 due to the combination of hardness and toughness [51,52]. However, in this work, superhard yet tough Ti-C-N coatings provide excellent seawater lubrication with an ultralow COF of 0.03.

#### 4. Conclusion

In conclusion, we have demonstrated that superhard yet tough Ti-C-N coatings with mixed TiC and TiN phases were deposited by high-power impulse magnetron sputtering by precise control of average target power and negative substrate bias. Superhard yet tough Ti-C-N coatings exhibit the enhanced water-lubricating performance in 3.5 wt % NaCl aqueous solution with an extremely low coefficient of friction of 0.03 and a stable open circuit potential of  $-0.05$  V. The increased surface wettability and the resistance to crack initiation and propagation and adhesion failure contribute to the increased tribocorrosion resistance properties of superhard yet tough Ti-C-N coatings.

#### CRediT authorship contribution statement

1. Y.X. Ou contributes for the conceptualization, methodology, partial data processing, writing, revision and main funding support in this work.
2. H.Q. Wang completes coating depositions, test and analysis of samples.
3. Q.S. Hua and B. Liao offer experiment resources and partly funding support.

4. X.P. Ouyang contributes for data curation and discussion.

## Declaration of competing interest

The authors declare no competing interests.

## Acknowledgments

This work was supported by 2020 Mengya talent plan (Grant No. BGS202009) and Research start-up funds (Grant No. BS202024) granted by Beijing Academy of Science and Technology and from Changzhi Medical College, respectively. Besides, this work is also partly supported by Guangdong Province Key Area Research and Development Program (Grant No. 2019B090909002).

## References

- Z.L. Zhang, T. Bell, Structure and corrosion resistance of plasma nitrided stainless steel, *Surf. Eng.* 1 (1985) 131.
- R.J.K. Wood, Tribo-corrosion of coatings, *J. Phys. D. Appl. Phys.* 40 (2007) 5502.
- R.J.K. Wood, Marine wear and tribocorrosion, *Wear* 376–377 (2017) 893–910.
- Y.X. Ou, H.Q. Wang, B. Liao, M.K. Lei, X.P. Ouyang, Tribological behaviors in air and seawater of CrN/TiN superlattice coatings irradiated by high-intensity pulsed ion beam, *Ceram. Int.* 45 (2019) 24405.
- Q. Chen, Y. Cao, Z. Xie, T. Chen, Y. Wan, H. Wang, X. Gao, Y. Chen, Y. Zhou, Y. Guo, Tribocorrosion behaviors of CrN coating in 3.5 wt% NaCl solution, *Thin Solid Films* 622 (2017) 41.
- Q.Z. Wang, F. Zhou, K.M. Chen, M.L. Wang, T. Qian, Friction and wear properties of TiCN coatings sliding against SiC and steel balls in air and water, *Thin Solid Films* 519 (2011) 4830.
- T. Shao, F.F. Ge, C. Pei, F. Huang, D. Sun, S. Zhang, Effects of Si content on tribocorrosion behavior of Cr<sub>1-x</sub>Si<sub>x</sub>N coatings prepared via magnetron sputtering, *Surf. Coat. Technol.* 356 (2018) 11.
- Y.X. Wang, J.W. Zhang, S.G. Zhou, Y.C. Wang, C.T. Wang, Y.X. Wang, Y.F. Sui, J. B. Lan, Q.J. Xue, Improvement in the tribocorrosion performance of CrCN coating by multilayered design for marine protective application, *Appl. Surf. Sci.* 528 (2020), 147061.
- H.Q. Wang, Y.X. Ou, B. Liao, X.D. Ou, J. Luo, P. Pang, L. Chen, X. Zhang, Q.S. Hua, M.Y. Bao, Tribocorrosion behaviors of TiSiCN nanocomposite coatings deposited by high power impulse magnetron sputtering, *Mater. Res. Express.* 7 (2020), 076407.
- A. Hatema, J.L. Lin, R.H. Wei, R.D. Torres, C. Laurindo, G.B. Souza, P. Soares, Tribocorrosion behavior of low friction TiSiCN nanocomposite coatings deposited on titanium alloy for biomedical applications, *Surf. Coat. Technol.* 347 (2018) 1.
- A. Salicio-Paz, A. Dalmau, H. Grande, A. Iriarte, J. Sort, E. Pellicer, J. Fornell, E. García-Lecina, Impact of the multilayer approach on the tribocorrosion behaviour of nanocrystalline electroless nickel coatings obtained by different plating modes, *Wear* 456–457 (2020), 203384.
- S. Zhang, H.L. Wang, S.E. Ong, D. Sun, X.L. Bui, Hard yet tough nanocomposite coatings present status and future trends, *Plasma Process. Polym.* 4 (2007) 219.
- D. Jiang, Recent progresses in the phenomenological description for the indentation size effect in microhardness testing of brittle ceramics, *J. Adv. Ceram.* 1 (2012) 38.
- Y.X. Ou, X.P. Ouyang, B. Liao, X. Zhang, S. Zhang, Hard yet tough CrN/Si<sub>3</sub>N<sub>4</sub> multilayer coatings deposited by the combined deep oscillation magnetron sputtering and pulsed dc magnetron sputtering, *Appl. Surf. Sci.* 502 (2020), 144168.
- A. Matthews, S. Franklin, K. Holmberg, Tribological coatings: contact mechanisms and selection, *J. Phys. D. Appl. Phys.* 40 (2007) 5463.
- T. Vitu, A. Escudeiro, T. Polcar, A. Cavaleiro, Sliding properties of Zr-DLC coatings: the effect of tribolayer formation, *Surf. Coat. Technol.* 258 (2014) 734.
- S. Wilson, A.T. Alpas, Tribo-layer formation during sliding wear of TiN coatings, *Wear* 245 (2000) 223.
- Y.W. Ye, Y.X. Wang, H. Chen, J.L. Li, Y.R. Yao, C.T. Wang, Doping carbon to improve the tribological performance of CrN coatings in seawater, *Tribol. Int.* 90 (2015) 362.
- N.L. Bozec, C. Compère, M. L'Her, A. Laouenan, D. Costa, P. Marcus, Influence of stainless steel surface treatment on the oxygen reduction reaction in seawater, *Corros. Sci.* 43 (2001) 765.
- X.J. Yang, C.W. Du, H.X. Wan, Z.Y. Liu, X.G. Li, Influence of sulfides on the passivation behavior of titanium alloy TA2 in simulated seawater environments, *Appl. Surf. Sci.* 458 (2018) 198.
- J.L. Lin, B. Wang, Y.X. Ou, W.D. Sproul, I. Dahan, J.J. Moore, Structure and properties of CrSiN nanocomposite coatings deposited by hybrid modulated pulsed power and pulsed dc magnetron sputtering, *Surf. Coat. Technol.* 216 (2013) 251.
- D. Cavaleiro, S. Carvalho, A. Cavaleiro, F. Fernandes, TiSiN(Ag) films deposited by HIPIMS working in DOMS mode: effect of Ag content on structure, mechanical properties and thermal stability, *Appl. Surf. Sci.* 478 (2019) 426.
- Y.X. Ou, J.L. Lin, S. Tong, H.L. Che, W.D. Sproul, M.K. Lei, Wear and corrosion resistance of CrN/TiN superlattice coatings deposited by a combined deep oscillation magnetron sputtering and pulsed dc magnetron sputtering, *Appl. Surf. Sci.* 351 (2015) 332.
- Y.P. Purandare, G.L. Robinson, A.P. Eghasarian, P.E. Hovsepian, Investigation of high power impulse magnetron sputtering deposited nanoscale CrN/NbN multilayer coating for tribocorrosion resistance, *Wear* 452–453 (2020), 203312.
- M.M. Deng, J.J. Li, C.H. Zhang, J. Ren, N.N. Zhou, J.B. Luo, Investigation of running-in process in water-based lubrication aimed at achieving super-low friction, *Tribol. Int.* 102 (2016) 257.
- L. Shan, Y.X. Wang, J.L. Li, H. Li, X.D. Wu, J.M. Chen, Tribological behaviours of PVD TiN and TiCN coatings in artificial seawater, *Surf. Coat. Technol.* 226 (2013) 40.
- O.J. Akinribide, B.A. Obadele, S.O. Akinwamide, H. Bilal, O.O. Ajibola, O. O. Ayeleru, S.P. Ringer, P.A. Olubambi, Sintering of binderless TiN and TiCN-based cermet for toughness applications: processing techniques and mechanical properties, *Ceram. Int.* 45 (2019) 21077.
- J. Xu, L.L. Liu, P. Munroe, Z.H. Xie, Z.T. Jiang, The nature and role of passive films in controlling the corrosion resistance of MoSi<sub>2</sub>-based nanocomposite coatings, *J. Mater. Chem. A* 1 (2013) 10281.
- J. Klein, Hydration lubrication, *Friction*. 1 (2013) 1.
- H.C. Liu, F. Guo, P.L. Wong, X. Li, Investigation of adsorbed protein and passive films on hydrodynamic lubricated steel slider surface, *Tribol. Int.* 109 (2017) 133.
- J. Luo, Y.X. Ou, Z.Q. Zhang, P. Pang, L. Chen, B. Liao, H.Z. Shang, X. Zhang, X. Y. Wu, Low friction coefficient of superhard nc-TiC/a-C:H nanocomposite coatings deposited by filtered cathodic vacuum arc, *Mater. Res. Express.* 6 (2019), 096418.
- Verein Deutscher Ingenieure Normen, VDI 3198, VDI verlag, 1991.
- D.B. Marshall, B.R. Lawn, A.G. Evans, Elastic/plastic indentation damage in ceramics: the lateral crack system, *J. Am. Ceram. Soc.* 65 (1982) 561.
- X. Tian, J.T. Korhonen, R.H.A. Ras, T. Huhtamäki, Surface-wetting characterization using contact-angle measurements, *Nat. Protoc.* 13 (2018) 1521.
- J.L. Lin, W.D. Sproul, J.J. Moore, Z.L. Wu, S. Lee, R. Chistyakov, B. Abraham, Recent advances in modulated pulsed power magnetron sputtering for surface engineering, *JOM* 63 (2011) 48.
- A. Belosludtsev, J. Vlček, J. Houška, S. Haviar, R. Čerstvý, Tunable composition and properties of Al-O-N films prepared by reactive deep oscillation magnetron sputtering, *Surf. Coat. Technol.* 392 (2020), 125716.
- M.A. Lieberman, A.J. Lichtenberg, Principles of Plasma Discharge and Materials Processing, 2nd Edition, 2005.
- G.F. Zheng, Q. Jiao, C. Li, Y. Ding, J.N. He, Y.F. Jiang, H.J. Zhao, Influence of nitridation on the microstructure and corrosion behavior of reactive plasma sprayed TiCN coatings, *Surf. Coat. Technol.* 396 (2020), 125954.
- Q.Z. Wang, F. Zhou, S. Gao, Z.F. Zhou, L.K.Y. Li, J.W. Yan, Effect of counterparts on the tribological properties of TiCN coatings with low carbon concentration in water lubrication, *Wear* 328–329 (2015) 356.
- Y.X. Ou, H. Chen, Z.Y. Li, J. Lin, W. Pan, M.K. Lei, Microstructure and tribological behavior of TiAlSiN coatings deposited by deep oscillation magnetron sputtering, *J. Am. Ceram. Soc.* 101 (2018) 5166.
- J. Lin, J.J. Moore, B. Mishra, M. Pinkas, W.D. Sproul, The structure and mechanical and tribological properties of TiBCN nanocomposite coatings, *Acta Mater.* 58 (2010) 1554.
- A. Anders, A structure zone diagram including plasma-based deposition and ion etching, *Thin Solid Films* 518 (2010) 4087.
- Y.X. Ou, J. Lin, H.L. Che, W.D. Sproul, J.J. Moore, M.K. Lei, Mechanical and tribological properties of CrN/TiN multilayer coatings deposited by pulsed dc magnetron sputtering, *Surf. Coat. Technol.* 276 (2015) 152.
- R. Chen, J.P. Tu, D.G. Liu, Y.J. Mai, C.D. Gu, Microstructure, mechanical and tribological properties of TiCN nanocomposite films deposited by DC magnetron sputtering, *Surf. Coat. Technol.* 205 (2011) 5228.
- M. Lei, X.P. Zhu, D.M. Guo, Reducing geometrical, physical, and chemical constraints in surface integrity of high-performance stainless steel components by surface modification, *J. Manuf. Sci. E-T. Asme*. 138 (2016), 044501.
- M. Samuelsson, D. Lundin, J. Jensen, M.A. Raadu, J.T. Gudmundsson, U. Helmersson, On the film density using high power impulse magnetron sputtering, *Surf. Coat. Technol.* 205 (2010) 591.
- L. Li, L. Liu, X. Li, P. Guo, P. Ke, A. Wang, Enhanced tribocorrosion performance of Cr/GLC multilayered films for marine protective application, *ACS. Appl. Mater. Interface* 10 (2018) 13187.
- E.K. Bobzin, The influence on surface free energy of PVD-coatings, *Surf. Coat. Technol.* 142–144 (2001), 755.
- T. Young, An essay on the cohesion of fluids, *Philos. Trans. R. Soc. Lond.* 95 (1805) 65.
- J. Song, D.L. Zeng, L.W. Fan, Temperature dependence of contact angles of water on a stainless steel surface at elevated temperatures and pressures: in situ characterization and thermodynamic analysis, *J. Colloid. Interf. Sci.* 561 (2020) 870.
- J. Zhang, Y. Wang, S. Zhou, Y. Wang, C. Wang, W. Guo, X. Lu, L. Wang, Tailoring self-lubricating, wear-resistance, anticorrosion and antifouling properties of Ti/(Cu, MoS<sub>2</sub>)-DLC coating in marine environment by controlling the content of Cu dopant, *Tribol. Int.* 143 (2020) 106029.
- L. Cao, J. Liu, Y. Wan, J. Pu, Corrosion and tribocorrosion behavior of W doped DLC coating in artificial seawater, *Diamond. Relat. Mater.* 109 (2020), 108019.